Sustainable Energy & Fuels

ROYAL SOCIETY OF CHEMISTRY

PAPER

View Article Online
View Journal

Cite this: DOI: 10.1039/d5se01611h

Hybrid iodobismuthates formed by mechanochemical synthesis as pseudocapacitor electrode materials

Yishan Lu, Caroline Kirk* and Neil Robertson *

Supercapacitors, as a complementary type of energy storage device between secondary batteries and conventional capacitors, show the advantages of high-power density and stable cyclability. However, there are still challenges that remain to be solved, such as their relatively low energy density compared with secondary batteries. Herein, we report a new class of materials for supercapacitors, specifically two organic/inorganic hybrid iodobismuthate materials, 2-aminothiazolium bismuth iodide ([AT][BiI_4]) and tetrabutylammonium bismuth iodide ([TBA]$_3$[Bi_3I_{12}]). Both materials were synthesised by mechanochemistry, which is a green route with lower energy and resource consumption compared with solution-based methods. [TBA]$_3$[Bi_3I_{12}] was also synthesised by precipitation for comparison. We tested the electrochemical performance of these materials using a three-electrode system and bismuth was shown to provide the redox active centre. The results illustrate that the mechanochemically-synthesised materials have higher performance, which suggests that further study of mechanochemical synthesis for hybrid iodobismuthates would be fruitful.

Received 5th December 2025
Accepted 23rd March 2026

DOI: 10.1039/d5se01611h

rsc.li/sustainable-energy

1 Introduction

The 21st century is dominated by internet and electronic technology, leading to a substantial expansion of the electronic products market.[1] At the same time, renewable energy alternatives to fossil fuels face challenges due to their intermittent energy supply.[2] Energy storage devices, including batteries, fuel cells and electrochemical supercapacitors, are therefore set to play a crucial role in the renewable energy supply system. When compared to secondary batteries, the energy storage of supercapacitors is relatively limited,[3,4] however they have the advantage of fast charge and discharge. In the pursuit of supercapacitors with higher performance and lower cost, research has strongly focused on improving the electrode materials.

Recently, Bi-based materials have attracted interest as promising candidates for energy storage materials because of their high theoretical specific capacity and good conductivity.[5–7] Bi-based materials are non-toxic and exhibit high chemical stability, with applications found in various energy storage device contexts including study as supercapacitor electrodes.[8–11] According to previous work on BiSI,[12] Bi has been shown to be the redox-active centre, giving a pseudocapacitor mechanism that can boost the storage. Additionally, hybrid organic–inorganic structures offer potential for discovering new materials. Several such hybrid iodobismuthate materials have been reported as electrode materials in energy storage devices. Popoola *et al.*[13] fabricated a photo-supercapacitor using methylammonium bismuth triiodide, exhibiting exceptional cyclability, retaining 94.79% of its initial capacitance after 5000 CV cycles. Pious *et al.*[14] synthesised zero-dimensional $(CH_3NH_3)_3Bi_2I_9$ for electric double layer capacitors (EDLC); an areal capacitance of 5.5 mF cm^{-2} was achieved and 84.8% retention was observed after 10 000 cycles. To date, there has been limited further study into iodobismuthates as materials for supercapacitor applications.

[AT][BiI_4] (2-amonithiazolium bismuth iodide) has been studied as an electrode material for lithium-ion batteries, with reversible Li-ion capacity of 520 mAh g^{-1} under 250 charge–discharge cycles at an applied current density of 0.1 A g^{-1}.[10] In this work, we study [AT][BiI_4] as a supercapacitor anode. Schematic crystal structure diagrams of [AT][BiI_4] are shown in Fig. 1(a), from the Cambridge Structural Database.[15] [AT][BiI_4] contains aromatic heterocycle 2-aminothiazole as a cation, and the structure consists of edge-sharing chains of [BiI_6] octahedra surrounded by aminothiazolium cations. For comparison, we also chose [TBA]$_3$[Bi_3I_{12}] (tetrabutylammonium bismuth iodide) to explore the viability of using a similar hybrid material with an aliphatic cation for supercapacitor electrodes. Two published [TBA]$_3$[Bi_3I_{12}] structures, a monoclinic phase[16] and a triclinic phase,[17] are reported. The crystal structure of the monoclinic polymorph is shown in Fig. 1(b) and the triclinic one in Fig. 1(c) and (d). In monoclinic [TBA]$_3$[Bi_3I_{12}], each unit cell consists of face-sharing [BiI_6] octahedra with 3 Bi atoms in the asymmetric unit surrounded by tetrabutylammonium cations, while the triclinic polymorph contains face-sharing [BiI_6] octahedra with

EaStChem School of Chemistry, University of Edinburgh, David Brewster Road, King's Buildings, Edinburgh EH9 3FJ, UK. E-mail: Y.Lu-123@sms.ed.ac.uk; Caroline.Kirk@ed.ac.uk; Neil.Robertson@ed.ac.uk

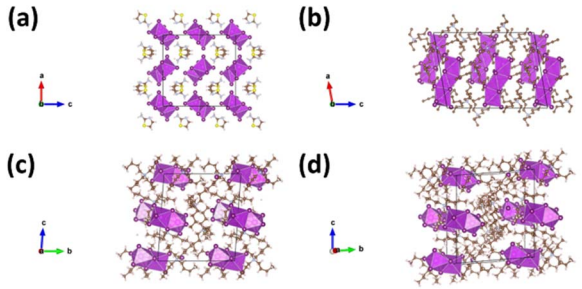

Fig. 1 (a) *ac* projection of AT[BiI_4] showing edge-sharing pairs of BiI_6 octahedra,[18] (b) *ac* projection of monoclinic [TBA]$_3$[Bi_3I_{12}] showing face sharing BiI_6 polyhedral forming Bi_3I_{12} chains running along the *a* direction,[16] (c) and (d) *bc* pseudo-projection and perspective view of triclinic [TBA]$_3$[Bi_3I_{12}] showing face-sharing pairs of BiI_6 octahedra forming Bi_2I_9 units,[17] red octahedra: BiI_6, yellow sphere: I; purple sphere (C), orange sphere (H), cyan sphere (N), pink sphere (S). The diagram was created using the crystal structure visualization software VESTA.[19]

3 Bi atoms between two asymmetric units surrounded by tetrabutylammonium cations.

Mechanochemical synthesis has emerged as a promising approach for synthesising materials.[20] This method offers several advantages compared to commonly used solution-based processes, including lower toxicity, as organic solvents are not used or are used in small quantities, ease of implementation and the minimal formation of side products, bringing potential for the synthesis of energy storage materials.[21–23] Mechanochemistry involves activating chemical reactions through the application of mechanical energy, which can be generated through various forces and operation modes such as impact, compression, or shear. Mechanochemical synthesis can be carried out using simple equipment such as a mortar and pestle, or with more advanced equipment such as shaking or planetary ball mills, as well as mechanical grinding in twin-screw extruders. Recently, mechanochemical synthesis has been applied to the preparation of hybrid iodobismuthate compounds for X-ray detection applications.[24] However, to the best of our knowledge, this is the first report applying mechanochemical synthesis to prepare hybrid iodobismuthates as electrode materials for energy storage devices, aiming to explore the feasibility of mechanochemistry as a synthesis route for new electrode materials.

We discuss the synthesis and characterisation of 2-aminothiazolium bismuth iodide ([AT][BiI_4]) and tetrabutylammonium bismuth iodide ([TBA]$_3$[Bi_3I_{12}]). For comparison, the synthesis of [TBA]$_3$[Bi_3I_{12}] was carried out using both precipitation ([TBA]$_3$[Bi_3I_{12}]_P) and mechanochemical methods ([TBA]$_3$[Bi_3I_{12}]_G).

2 Experimental

2.1 Materials

2-Aminothiazole ($C_3H_4N_2S$, 97%, Sigma-Aldrich), hydroiodic acid (HI, 57 wt% in H_2O, Sigma-Aldrich), bismuth(III) iodide (BiI_3, 98%, TCI Chemicals), tetrabutylammonium iodide ($C_{16}H_{36}NI$, 98%, Sigma-Aldrich), dimethyl sulfoxide (C_2H_6SO, extra pure, Fisher Scientific) and potassium hydroxide (KOH, Fisher Scientific) were used without any further purification.

2.2 Synthesis method

[AT][BiI_4]: (Fig. S3) the precursor 2-aminothiazolium iodide. (ATI) was prepared according to the reported procedure,[18] and characterised by ^{1}H-NMR (SI) and CHNS elemental analysis (Table S1). 2-Aminothiazolium bismuth iodide ([AT][BiI_4]) was obtained by a mechanochemical method. ATI pale yellow powder (0.0575 g, 0.25 mmol) and bismuth(III) iodide black powder (0.1474 g, 0.25 mmol) were mixed in an agate mortar, approximately 2 drops of ethanol were added. After 15 min of hand grinding, a dark pink powder (yield 0.1812 g, 90.42%) formed, which was initially shown to have the formula [$C_3H_5N_2S$][BiI_4] by elemental analysis and Inductively Coupled Plasma Mass spectroscopy (ICP-MS), shown in Tables S2 and S3.

[TBA]$_3$[Bi_3I_{12}]_P: (Fig. S4) tetrabutylammonium iodide white powder (0.0923 g, 0.25 mmol) and bismuth(III) iodide black powder (0.1470 g, 0.25 mmol) were separately dissolved in 5 and 15 mL ethanol respectively. Both solutions were filtered using 1.0 mL syringe and 22 μm PTFE syringe filter and subsequently mixed dropwise into a 28 mL vial. The mixed solution turned bright orange, and the vial was sealed with parafilm to avoid dust and other impurities. Holes were pierced in the parafilm, and it was left at room temperature for 7 days. An orange solid precipitated in the bottom and the remaining solution was transparent and light yellow. The orange precipitate, sample [TBA]$_3$[Bi_3I_{12}]_P (yield 0.1382 g, 57.76%) was calculated to have the chemical formula [$(C_4H_9)_4N$]$_3$[Bi_3I_{12}] by elemental analysis (Table S4).

[TBA]$_3$[Bi_3I_{12}]_G: (Fig. S5) tetrabutylammonium iodide white powder (0.0742 g, 0.2 mmol) and bismuth(III) iodide black powder (0.1178 g, 0.2 mmol) were mixed in an agate mortar, and approximately 2 drops of DMSO were added dropwise. After 15 min of grinding by hand, an orange powder (0.1625 g, 84.66%) formed, labelled [TBA]$_3$[Bi_3I_{12}]_G. The elemental analysis result is shown in Table S5.

2.3 Characterisation

NMR spectra were collected using a Bruker ava500 spectrometer. Powder X-ray diffraction (PXRD) data were collected on the Rigaku MiniFlex benchtop X-ray diffractometer in reflection geometry with a HyPix-400 MF 2D hybrid pixel array detector over the 5–50° 2θ for 15 minutes. PXRD data were analysed through comparison with the ICSD database. High resolution PXRD data were collected using a Rigaku Smartlab XE X-ray Powder diffractometer in reflection geometry with Cu Kα_1 radiation (λ = 1.54056 Å). A HyPix-400 semiconductor pixel array detector, was used to collect data over the 2θ range 5–50° 2θ for [AT][BiI_4], [TBA]$_3$[Bi_3I_{12}]_P and [TBA]$_3$[Bi_3I_{12}]_G. Samples were prepared as thin smears on a silicon substrate. Scanning Electron Microscopy (SEM) images were captured by ThermoScientific Phenom G6 Pure Scanning Electron Microscope, and the acceleration voltage was set as 10 kV. CHNS elemental analysis was carried out by Mettler Toledo high precision scale and ThermoFlash 2000. ICP-MS uses a plasma source that

ionises most elements in the range of 0–240 amu into singly charged positive ions (M^+).

2.4 Electrode fabrication

All coated electrodes used nickel foam (NF) as the current collector. To prevent oxidation on the NF surface, pre-treatments were carried out prior to electrode coating. The NF was cut into 1 × 2 cm pieces and successively cleaned with acetone, 1 M HCl solution, ultrapure water, and ethanol, each for 15 minutes, and were dried in the 100 °C vacuum oven overnight. The dried NF pieces were weighed and the mass recorded as m for future calculation. The electrode coating process involved the preparation of a paste consisting of the electrode active material, conductive agent, and binder, mixed together in a mass ratio of 8 : 1 : 1. For the bismuth-complex electrode, carbon black Super P served as the conductive agent, while a 5% carboxymethyl cellulose (CMC) solution (in H_2O) acted as the binder. These components were mixed with a few drops of ultrapure water to create a black, thick paste and coated onto NF pieces using a spatula. The well-coated NF pieces were then dried overnight in a 60 °C vacuum oven. The dried NF pieces were placed on a tablet press and pressed at a force of 10 MPa for 1 min.

Afterwards, the NF sheets were weighed, and their mass recorded as m_{Bi} for the bismuth-complex electrode. To determine the actual loading of the active substance coated on the electrode sheets, formula (1) was used:

$$M = 0.8 \times (m_{Bi} - m) \quad (1)$$

2.5 Three-electrode system setup and electrochemical measurement

The three samples, [AT][BiI_4], [TBA]$_3$[Bi_3I_{12}]_P and [TBA]$_3$[Bi_3I_{12}]_G were tested under a three-electrode assembly, using an Autolab electrochemical workstation with GPES software. The working electrode consisted of a nickel foam sheet coated with the active material, with a test area of 1 × 1 cm. In the test of [AT][BiI_4], the reference electrode used was a silver/silver chloride electrode (Ag/AgCl, E (*vs.* SHE) = E (*vs.* Ag/AgCl) + 0.22), while mercury/mercury oxide (Hg/HgO, E (*vs.* SHE) = E (*vs.* Hg/HgO) + 0.10) was used in the test of [TBA]$_3$[Bi_3I_{12}]_P and [TBA]$_3$[Bi_3I_{12}]_G. The counter electrode was a platinum sheet electrode with an area of 1 × 1 cm. The electrolyte solution was 1 M KOH.

The specific capacitance value of the electrode materials can be calculated by using the formula (2) below:

$$C_s = A/(2 \times m \times \Delta V \times k) \quad (2)$$

where C_s (F g^{-1}) is the specific capacitance, A is the integral area under CV curve (calculated using Origin software), ΔV (V) is the potential window range, m (g) is the mass of active material load (excluding binder, conductive agent and current collector), k (V s^{-1}) is the scan rate.

Under the galvanostatic charge–discharge (GCD) test, the results can be used to calculate the specific capacity C_p of the electrode material using formula (3):

$$C_p = I \times \Delta t/m \quad (3)$$

where C_p (C g^{-1}) is specific capacity of electrode material, I (A) is the current, Δt (s) is the discharge time, and m (g) is the mass of the active material (excluding binder, conductive agent and current collector) coated on the electrode.

In this study, electrochemical impedance frequency scans were conducted over the range 0.01 Hz to 100 kHz, with an amplitude of ±10 mV at an open circuit potential of 0 V. The equivalent circuit was simulated on the ZView and ZPlot software. The Bode plot is depicted based on the calculation of φ and $|Z|$ in Origin. The fitted result based on the equivalent circuit is inserted in both Nyquist plot and Bode plot pictures.

3 Results and discussion

[AT][BiI_4], [TBA]$_3$[Bi_3I_{12}]_P and [TBA]$_3$[Bi_3I_{12}]_G were successfully synthesised using the procedures outlined in the Experimental section, followed by the characterisation and electrochemical tests outlined below.

3.1 Characterisation

Powder X-ray diffraction (PXRD) data were collected on the samples to identify the phase(s) present (Fig. 2). The high resolution PXRD data were refined using a Pawley fitting routine in the software Topas Academic,[25] using the published unit cell parameters as the starting values. As shown in Fig. 2(a), [TBA]$_3$[Bi_3I_{12}]_P matches well to the monoclinic [TBA]$_3$[Bi_3I_{12}] polymorph.[16] The unit cell parameters were refined in space group $P2_1/c$, with a = 17.789 (6) Å, b = 20.545 (7) Å, c = 23.344 (8) Å, β = 100.16 (3)°. The PXRD data collected on [TBA]$_3$[Bi_3I_{12}]_G is shown in Fig. 2(b) and on analysis the monoclinic and triclinic polymorphs were both identified as present. A Pawley fit of the PXRD data using both polymorphs was carried out and the refined unit cell parameters were calculated for comparison with published data of both monoclinic[16] and triclinic polymorphs.[17] The refined unit cell parameters are in the monoclinic space group $P2_1/c$, a = 17.704 (7) Å, b = 20.224 (7) Å, c = 23.17 (1) Å, β = 99.99 (3)°, and in the triclinic space group $P\bar{1}$, a = 11.866 (5) Å, b = 17.465 (8) Å, c = 19.428 (8) Å, α = 85.47 (4)°, β = 87.45 (5)°, γ = 79.45 (6)° which matches well to the published data (Table S6). This enables most of the observed peaks to be assigned to polymorphs of [TBA]$_3$[Bi_3I_{12}], which confirms the successful synthesis of [TBA]$_3$[Bi_3I_{12}] with both monoclinic and triclinic phases present. However, there is still at least one unassigned peak that doesn't match either of these two phases, which is observed in the datasets of both [TBA]$_3$[Bi_3I_{12}]_P and [TBA]$_3$[Bi_3I_{12}]_G (Fig. 2(c)). Comparison with the reference patterns of the starting reagents shows it is not due to the presence of either of these phases. Our hypothesis is that the extra peak indicates the presence of a small component of other minor phase(s), however the monoclinic and triclinic phase of [TBA]$_3$[Bi_3I_{12}] are the only two known phases to date. The PXRD

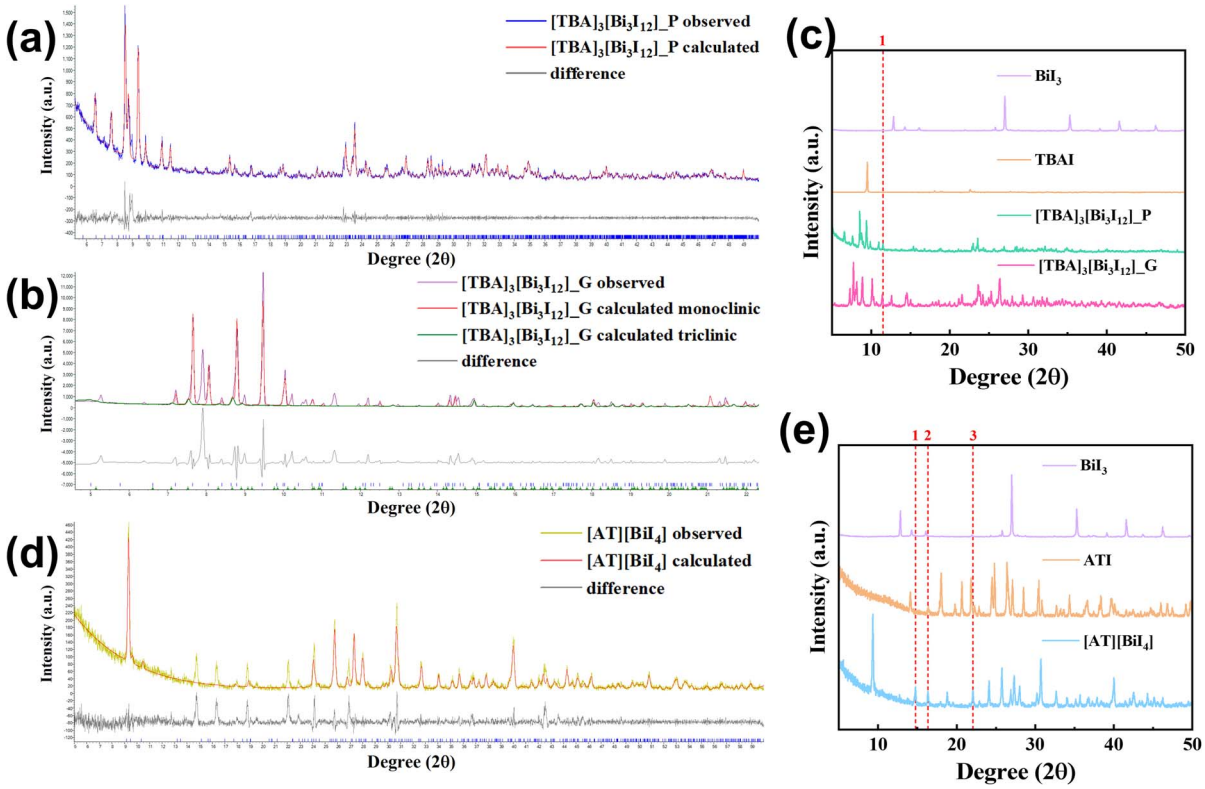

Fig. 2 PXRD pattern. (a) Observed (blue), calculated (red) and difference (black) plots from the Pawley fitting of $[TBA]_3[Bi_3I_{12}]$_P in the monoclinic crystal system; (b) observed (violet), calculated (red for monoclinic, green for triclinic) and difference (black) plots from the Pawley fitting of $[TBA]_3[Bi_3I_{12}]$_G to both the monoclinic and triclinic polymorphs (c) $[TBA]_3[Bi_3I_{12}]$_G (pink) compared to $[TBA]_3[Bi_3I_{12}]$_P (green) and reagent TBAI (orange) and BiI_3 (violet). The unassigned peak 1 at ~11.4° 2θ in both $[TBA]_3[Bi_3I_{12}]$_P and $[TBA]_3[Bi_3I_{12}]$_G is highlighted by the red dotted line in the picture. (d) Observed (yellow), calculated (red) and difference (black) plots from the Pawley fitting of $[AT][BiI_4]$ in the orthorhombic crystal system. (e) $[AT][BiI_4]$ (cyan blue) compared to reagent ATI precursor (orange) and BiI_3 (violet). The unassigned peaks 1, 2, 3 at ~14.7, 16.3, 22.1° 2θ are highlighted by the red dotted line in the picture.

data collected on $[AT][BiI_4]$ (Fig. 2(d)) was refined in the orthorhombic space group *Pbca*, where $a = 18.619$ (3) Å, $b = 7.525$ (2) Å, $c = 19.250(5)$ Å, which matches well with the published parameters calculated from the orthorhombic $[AT][BiI_4]$ (Table S6).[18]

However, the presence of peaks highlighted as 1, 2, 3 in the figure of the PXRD pattern which cannot be assigned to this phase suggests the presence of possible minor impurity phases in the sample (Fig. 2(e)). Elemental analysis of $[AT][BiI_4]$ bulk sample using CHNS elemental analysis (Table S2) and ICP-MS (Table S3) confirms the proposed formula, which suggests the unassigned peaks after analysis of the PXRD data are due to, as yet, unknown polymorphs of $[AT][BiI_4]$. In general, any unidentified phases in these materials appeared as only minor peaks and the electrochemical performance will be dominated by the behaviour of the identified phases present. The SEM image Fig. 3(a) shows $[AT][BiI_4]$ contains non-uniform micron scale particles up to 5 μm. The size heterogeneity may be caused by uneven grinding during the synthesis. The particles are clustered together, potentially leading to less surface area and porosity. Fig. 3(b) presents the SEM image of $[TBA]_3[Bi_3I_{12}]$_P, which appears very crystalline, with needle-like crystals of around 100 μm. In contrast, we can see from Fig. 3(c) that $[TBA]_3[Bi_3I_{12}]$_G has a range of particle sizes from 1 to 10 μm, and the agglomeration of particles is severe. This may be related to the use of polar DMSO as solvent to assist the grinding. After the $[TBA]_3[Bi_3I_{12}]$_G has dried, the particles may become clustered and partially fused together.

3.2 Electrochemical performance

The $[AT][BiI_4]$ was tested in a three-electrode system over a potential window of −0.98 V to 0.22 V compared to the SHE reference, while $[TBA]_3[Bi_3I_{12}]$ samples were also tested over −0.9 V to 0.1 V. These show (Fig. 4) redox peaks in the CV curves and discharge plateaus in the GCD curves, demonstrating redox pseudocapacitive features. With increasing scan rate, the reduction peak shifts to more negative values while the oxidation peaks shift to more positive values, which is caused by increased IR drop and polarisation. In the CV curve of $[AT][BiI_4]$ (Fig. 4(a)), we can see two reduction peaks and two oxidation peaks at a scan rate of 5 mV s^{-1}, while at higher scan rate of 10 mV s^{-1} to 100 mV s^{-1}, there is only one oxidation peak together with two reduction peaks. The reduction peaks are located at around −0.75 V and −0.6 V, attributed to the reduction of Bi^{3+} to Bi^{+} then to Bi^{0}, while two oxidations are located at −0.35 V and −0.2 V, indicating the re-oxidation process of Bi^{0} to

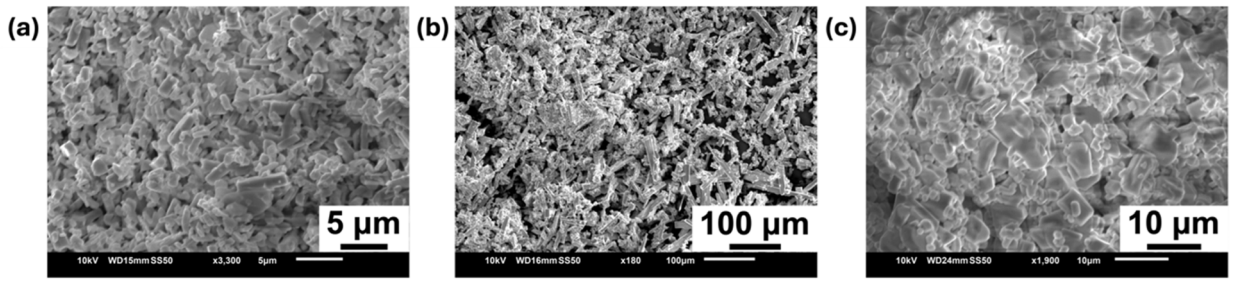

Fig. 3 SEM images (a) $[AT][BiI_4]$, (b) $[TBA]_3[Bi_3I_{12}]$_P, (c) $[TBA]_3[Bi_3I_{12}]$_G.

Bi^+ then to Bi^{3+}.[12,26,27] At the same time, the two oxidation peaks merged into one from scan rate of 10 mV s^{-1} and higher. A similar conclusion can be drawn from the GCD result showing two plateaus during the charging process and one plateau during the discharge (Fig. 4(b)). The discharge plateau is located around −0.4 V, where Bi is oxidised into Bi^{3+}. In the CV curves of

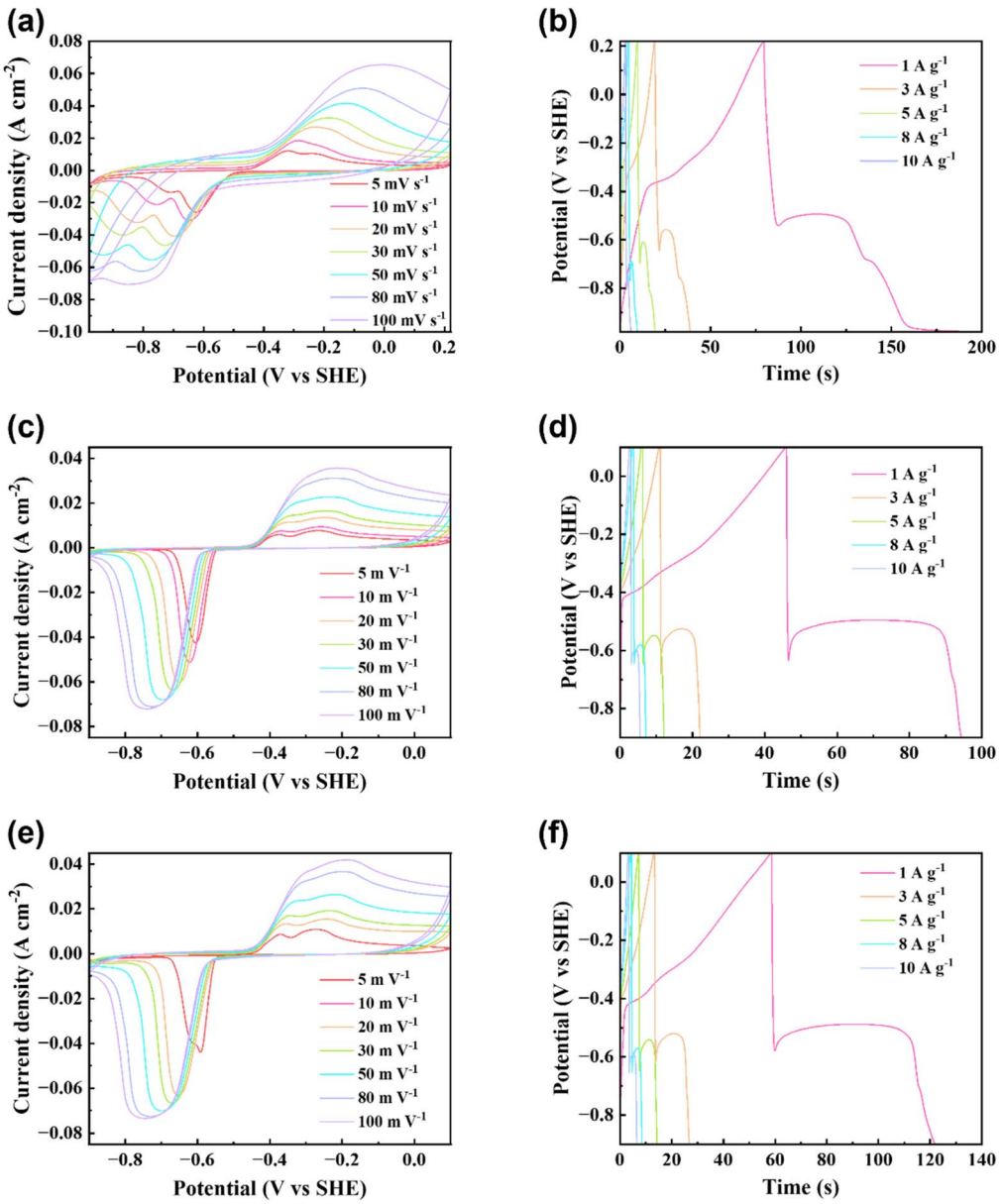

Fig. 4 CV at the scan rate from 5 mV s^{-1} to 100 mV s^{-1} of electrodes (a) $[AT][BiI_4]$, (c) $[TBA]_3[Bi_3I_{12}]$_P, (e) $[TBA]_3[Bi_3I_{12}]$_G; GCD curve under the current density from 1 A g^{-1} to 10 A g^{-1} of electrodes (b) $[AT][BiI_4]$, (d) $[TBA]_3[Bi_3I_{12}]$_P, (f) $[TBA]_3[Bi_3I_{12}]$_G.

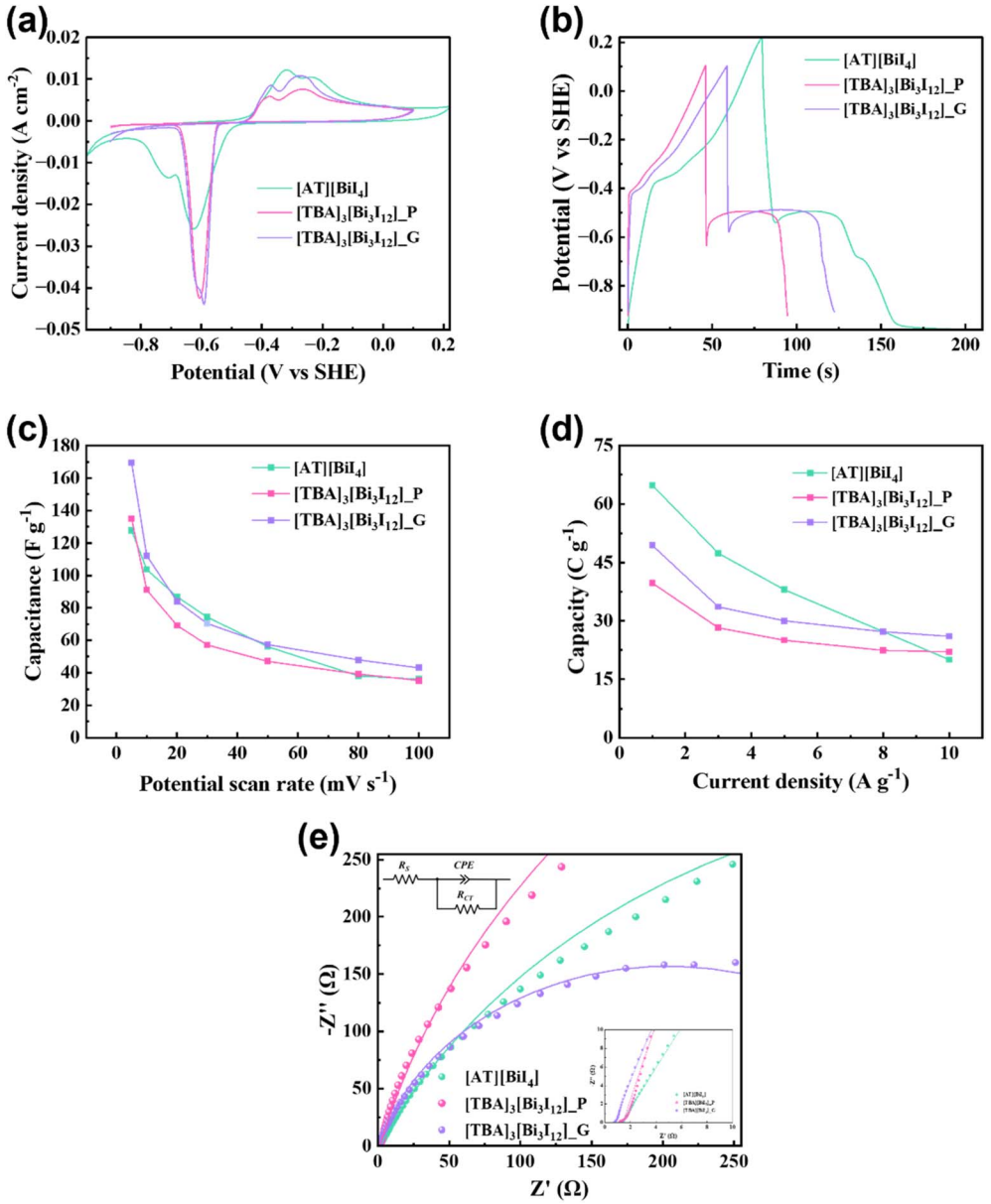

Fig. 5 Comparison of [AT][BiI$_4$] (orange line), [TBA]$_3$[Bi$_3$I$_{12}$]_P (green line), [TBA]$_3$[Bi$_3$I$_{12}$]_G (blue line): (a) CV at a scan rate of 5 mV s^{-1}; (b) GCD at a current density of 1 A g^{-1}; (c) specific capacitance based on the CV result; (d) specific capacity based on GCD result; (e) Nyquist plot.

both [TBA]$_3$[Bi$_3$I$_{12}$]_P and [TBA]$_3$[Bi$_3$I$_{12}$]_G (Fig. 4(c) and (e)), three peaks are observed: one reduction peak at approximately −0.6 V, indicating the reduction of Bi^{3+} to Bi^0, and two oxidation peaks at around −0.35 V and −0.2 V, implying the oxidation process from Bi^0 to Bi^+ and Bi^+ to Bi^{3+}.[26,27] Similar observations can be seen from the GCD results where one plateau emerged during discharge in Fig. 4(d) and (f). This plateau is at around −0.4 V and corresponds to Bi oxidation to Bi^{3+}. Overall, CV and GCD measurements demonstrate pseudocapacitive behaviour during the charge and discharge process, with reversible changes in the bismuth redox centre between $Bi^{3+} \rightleftharpoons Bi^+ \rightleftharpoons Bi^0$.

To give a further understanding of the electrode performance, we show comparison of the three materials in Fig. 5. In the CV curve at the scan rate of 5 mV s^{-1}, both [TBA]$_3$[Bi$_3$I$_{12}$]_P and [TBA]$_3$[Bi$_3$I$_{12}$]_G show a very sharp reduction peak at around −0.6 V (Fig. 5(a)), which suggests that the reactive sites are very accessible, while the reduction peak in [AT][BiI$_4$] is broader and divided into two steps. This corresponds to the GCD result in Fig. 5(b) at a current density of 1 A g^{-1}. The specific capacitances obtained from CV under different scan rates is shown in the Fig. 5(c). At 5 m V^{-1}, the specific capacitances of [AT][BiI4], [TBA]$_3$[Bi$_3$I$_{12}$]_P and [TBA]$_3$[Bi$_3$I$_{12}$]_G electrodes are 128 F g^{-1}, 125 F g^{-1} and 170 F g^{-1}, individually dropping to 36 F g^{-1}, 35 F g^{-1} and 43 F g^{-1} by 100 m V^{-1}. From the picture we can see that the capacitance of [TBA]$_3$[Bi$_3$I$_{12}$]_P, at every scan rate, is the lowest, and the [TBA]$_3$[Bi$_3$I$_{12}$]_G is the highest at 5 mV s^{-1} and 10 mV s^{-1}. [TBA]$_3$[Bi$_3$I$_{12}$]_P and [TBA]$_3$[Bi$_3$I$_{12}$]_G showed good specific capacitance suggesting

Table 1 The values and estimated errors (%) of [AT][BiI_4], [TBA]$_3$[Bi_3I_{12}]_P and [TBA]$_3$[Bi_3I_{12}]_G equivalent circuit elements. In the table, *R* stands for resistor and CPE means a constant phase element

Element	R_S (Ω)	Error (%)	R_{CT} (Ω)	Error (%)	CPE-Yo (F), CPE-N	Error (%)
[AT][BiI_4]	1.35	0.69	939.80	1.81	0.0024, 0.74	0.77, 0.24
[TBA]$_3$[Bi_3I_{12}]_P	1.41	1.27	1385	3.68	0.0018, 0.85	1.52, 0.44
[TBA]$_3$[Bi_3I_{12}]_G	0.77	0.78	405.80	2.45	0.0040, 0.84	1.13, 0.33

that exploring further similar compounds with aliphatic cations as electrode materials for supercapacitors would be worthwhile. The reason why [AT][BiI_4] has lower performance might be caused by low porosity discussed in the SEM section. As shown in the Fig. 5(d), the specific capacities of [AT][BiI_4], [TBA]$_3$[Bi_3I_{12}]_P and [TBA]$_3$[Bi_3I_{12}]_G electrodes are 65C g^{-1}, 40C g^{-1}, 50C g^{-1} at the energy density of 1 A g^{-1}, separately decreased into 20C g^{-1}, 22C g^{-1} and 26C g^{-1} by 10 A g^{-1}. We can also see in the current density of 1 to 8 A g^{-1}, [AT][BiI_4] is always the highest, followed by [TBA]$_3$[Bi_3I_{12}]_G and [TBA]$_3$[Bi_3I_{12}]_P subsequently. This shows the [TBA]$_3$[Bi_3I_{12}] materials would have a lower potential as battery material in aqueous system, since its energy density could be limited, while the good performance of [AT][BiI_4] might indicate its possibility as battery electrode, which corresponds to the result from previous study.[10]

To further investigate the electrochemical process, EIS was conducted with data presented as Nyquist (Fig. S9(a), (c) and (e)) and Bode plots (Fig. S9(b), (d) and (f)). Based on the results, the equivalent circuit was simulated by using the software package ZView and Zplot. A summary of the values and uncertainties of each element in the equivalent circuit of one parallel resistor and capacitor is listed in Table 1. A comparison of Nyquist plot results of the three materials is shown in Fig. 5(e). All three materials possess a small series resistance associated with electrolyte resistance, wires, clips or other contacts, evident as the intercept on the $-Z'$ axis. We can see a common feature that all these three materials have a quasi-semicircle in this frequency range, related to their faradaic charge transfer process.

[TBA]$_3$[Bi_3I_{12}]_G has the smallest R_{CT}, which was reflected by the shortest diameter of quasi-semicircle, and the highest CPE-N, indicating quickest charge transfer and a most ideal capacitor in the circuit among the three materials.

In addition, by comparing the performance of [TBA]$_3$[Bi_3I_{12}]_P and [TBA]$_3$[Bi_3I_{13}]_G, both the specific capacitance calculated from CV and the specific capacity calculated from GCD indicate that [TBA]$_3$[Bi_3I_{12}]_G is better than [TBA]$_3$[Bi_3I_{12}]_P, suggesting that the better electrochemical performance of [TBA]$_3$[Bi_3I_{12}]_G is due to the synthesis method. These observations confirm that [TBA]$_3$[Bi_3I_{12}]_G is the best candidate among three materials for a supercapacitor electrode material. Analysis of the SEM images showed [TBA]$_3$[Bi_3I_{12}]_G has a smaller crystalline size than [TBA]$_3$[Bi_3I_{12}]_P, which can contribute to a larger surface area. As the redox reaction in pseudocapacitive electrodes mostly happens on the electrode surface, it is important for the electrode materials to have a large surface area, which can be advantageous in improving the specific capacity. From the PXRD results presented earlier, where we have confirmed that the [TBA]$_3$[Bi_3I_{12}]_G sample is a mixture of monoclinic and triclinic [TBA]$_3$[Bi_3I_{12}] polymorphs while [TBA]$_3$[Bi_3I_{12}]_P only consists of the monoclinic [TBA]$_3$[Bi_3I_{12}] polymorph, there is the possibility that the presence of the triclinic [TBA]$_3$[Bi_3I_{12}] polymorph contributes to faster electron transfer. This could be explored by future work using a pure triclinic [TBA]$_3$[Bi_3I_{12}] polymorph sample as the electrode material and comparison of its electrochemical performance with [TBA]$_3$[Bi_3I_{12}]_P that contains only monoclinic [TBA]$_3$[Bi_3I_{12}] polymorph. Apart from the electrochemical performance, [TBA]$_3$[Bi_3I_{12}]_G also shows obvious advantages surpassing [TBA]$_3$[Bi_3I_{12}]_P concerning its synthesis method. First, the reaction time of mechanochemical method was reduced notably (15 min hand grinding *versus* days for the precipitation method) and the solvent quantity used was greatly reduced (negligible DMSO in [TBA]$_3$[Bi_3I_{12}]_G *versus* 15 mL ethanol in total in [TBA]$_3$[Bi_3I_{12}]_P), which contributes towards the drive to green chemistry and reduction in the amount of raw materials used during synthesis. Comparing their electrochemical performance under three-electrodes system, showed more favourable performance for the sample prepared *via* mechanochemical methods.

[TBA]$_3$[Bi_3I_{12}]_G has shown better pseudocapacitive performance than the precipitated analogue because of its larger surface area and faster charge transfer kinetics obtained by mechanochemical synthesis, which highlights the potential in using greener synthesis methods by replacing solution methods with mechanochemical methods for the formation of supercapacitor materials with improved electrochemical performance.

4 Conclusions

We successfully studied two hybrid iodobismuthate materials for their potential as electrode materials in supercapacitor applications. By comparing the electrochemical results of [AT][BiI_4] and [TBA]$_3$[Bi_3I_{12}], we have shown [AT][BiI_4] has better electrochemical performance as an electrode material. However, the performance of [AT][BiI_4] as a supercapacitor anode still requires improvement. We found [TBA]$_3$[Bi_3I_{12}] also shows good specific capacitance and thus opens up the potential in studying other aliphatic cation organic cations in hybrid electrode materials for supercapacitor applications. By comparing [TBA]$_3$[Bi_3I_{12}]_P and [TBA]$_3$[Bi_3I_{12}]_G, we can conclude that the mechanochemical method gave better electrochemical performance than the precipitation method for [TBA]$_3$[Bi_3I_{12}], suggesting wider scope for the replacement of

solution methods by mechanochemical methods when synthesising hybrid iodobismuthates.

For future work, studies into the formation and electrochemical characterisation of triclinic $[TBA]_3[Bi_3I_{12}]$ are required to investigate if this polymorph has improved electrochemical performance over the monoclinic polymorph as well as whether mixtures of the two polymorphs may have additional benefits.

Additionally, we can explore other iodobismuthates with aliphatic counterions to further explore the comparison between aliphatic cations and aromatic cations on the electrochemical performance. Furthermore, as Bi^{3+} provides a stable redox-active centre, these materials can be used in other energy storage devices, such as lithium-ion batteries and sodium-ion batteries.

Conflicts of interest

There are no conflicts to declare.

Data availability

The data supporting this article have been included as part of the supplementary information (SI). Supplementary information: characterisation data including elemental anayses; NMR; ICP-MS; PXRD; single-crystal XRD; EIS; electrochemical. See DOI: https://doi.org/10.1039/d5se01611h.

References

1 M. Liserre, T. Sauter and J. Y. Hung, *IEEE Ind. Electron. Mag.*, 2010, **4**, 18–37.
2 P. J. Hall and E. J. Bain, *Energy Policy*, 2008, **36**, 4352–4355.
3 P. Simon and Y. Gogotsi, *Nat. Mater.*, 2008, **7**, 845–854.
4 M. E. Şahin, F. Blaabjerg and A. Sangwongwanich, *Energies*, 2022, **15**, 674.
5 N. Devi and S. S. Ray, *Mater. Today Commun.*, 2020, **25**, 101691.
6 S. Yetiman, H. Peçenek, F. K. Dokan, S. Sanduvaç, M. Serdar Onses, E. Yılmaz and E. Sahmetlioglu, *Chemelectrochem*, 2024, **11**, e202300819.
7 E. Miniach and G. Gryglewicz, *J. Mater. Sci.*, 2018, **53**, 16511–16523.
8 D. Su, S. Dou and G. Wang, *Nano Energy*, 2015, **12**, 88–95.
9 H. Jung, C.-M. Park and H.-J. Sohn, *Electrochim. Acta*, 2011, **56**, 2135–2139.
10 K. Roy, T. Li, S. Ogale and N. Robertson, *J. Mater. Chem. A*, 2021, **9**, 2689–2693.
11 Y. Li, M. A. Trujillo, E. Fu, B. Patterson, L. Fei, Y. Xu, S. Deng, S. Smirnov and H. Luo, *J. Mater. Chem. A*, 2013, **1**, 12123–12127.
12 H. Sun, G. Yang, J. Chen, C. Kirk and N. Robertson, *J. Mater. Chem. C*, 2020, **8**, 13253–13262.
13 I. K. Popoola, M. A. Gondal, A. Popoola and L. E. Oloore, *J. Energy Storage*, 2022, **53**, 105167.
14 J. K. Pious, M. Lekshmi, C. Muthu, R. Rakhi and C. Vijayakumar, *ACS Omega*, 2017, **2**, 5798–5802.
15 C. R. Groom, I. J. Bruno, M. P. Lightfoot and S. C. Ward, *Struct. Sci.*, 2016, **72**, 171–179.
16 U. Geiser, E. Wade, H. H. Wang and J. Williams, *Cryst. Struct. Commun.*, 1990, **46**, 1547–1549.
17 S. Adonin, E. Peresypkina, M. Sokolov and V. Fedin, *J. Struct. Chem.*, 2015, **56**, 795–799.
18 T. Li, Q. Wang, G. S. Nichol, C. A. Morrison, H. Han, Y. Hu and N. Robertson, *Dalton Trans.*, 2018, **47**, 7050–7058.
19 K. Momma and F. Izumi, *J. Appl. Crystallogr.*, 2011, **44**, 1272–1276.
20 T. Friščić, C. Mottillo and H. M. Titi, *Angew. Chem.*, 2020, **132**, 1030–1041.
21 X. Liu, Y. Li, L. Zeng, X. Li, N. Chen, S. Bai, H. He, Q. Wang and C. Zhang, *Adv. Mater.*, 2022, **34**, 2108327.
22 N. Muralidharan, C. N. Brock, A. P. Cohn, D. Schauben, R. E. Carter, L. Oakes, D. G. Walker and C. L. Pint, *ACS Nano*, 2017, **11**, 6243–6251.
23 D. Tan and F. García, *Chem. Soc. Rev.*, 2019, **48**, 2274–2292.
24 A. Starkholm, D. Al-Sabbagh, S. Sarisozen, A. von Reppert, M. Rössle, M. Ostermann, E. Unger, F. Emmerling, L. Kloo and P. H. Svensson, *Adv. Mater.*, 2025, 2418626.
25 A. Coelho, Topas Academic: *General profile and structure analysis software for powder diffraction data*, Bruker AXS, Karlsruhe, Germany, 2012.
26 B. Sarma, A. L. Jurovitzki, Y. R. Smith, S. K. Mohanty and M. Misra, *ACS Appl. Mater. Interfaces*, 2013, **5**, 1688–1697.
27 V. Vivier, A. Régis, G. Sagon, J.-Y. Nedelec, L. Yu and C. Cachet-Vivier, *Electrochim. Acta*, 2001, **46**, 907–914.

